

Multiparticle $M1$ band in ^{134}La

Vinod Kumar and Pragya Das*

Physics Department, Indian Institute of Technology Bombay, Powai, Mumbai 400076, India

R. P. Singh, R. Kumar, S. Muralithar, and R. K. Bhowmik

Inter-University Accelerator Centre, Aruna Asaf Ali Marg, New Delhi 110067, India

(Received 6 December 2006; published 18 July 2007)

Lifetimes of seven low-lying excited states of ^{134}La in the picosecond range have been determined by the recoil distance method (RDM). Lifetimes of six states, belonging to a strong $M1$ band and having shorter lifetimes, have been determined by the Doppler shift attenuation method (DSAM). This band with intense $M1$ transitions and very few weak $E2$ crossovers appeared to be due to magnetic rotation. However, such a possibility is ruled out because roughly constant values of $B(M1)$ were found from the lifetime results. The semiclassical model was utilized to calculate the $B(M1)$ values; and after being compared with the experimental results, the band was assigned the multiparticle configuration $\pi g_{7/2} \otimes \nu h_{11/2}(h_{11/2})^2$, which differs from the earlier assignment of $\pi h_{11/2} \otimes \nu g_{7/2}(h_{11/2})^2$.

DOI: 10.1103/PhysRevC.76.014309

PACS number(s): 23.20.Lv, 21.10.Tg, 27.60.+j, 25.70.-z

I. INTRODUCTION

The nuclei in the mass region near 130 have drawn considerable attention in recent years. Depending on the configurations of the valence quasiparticles, rich and varied structural characteristics have been predicted and confirmed in a number of nuclei. Many nuclei [1,2] are γ soft and exhibit the shape coexistence phenomenon. Oblate bands have been observed in ^{131}La [3]. The most recent discovery has been the chiral doublet bands [4] and magnetic rotation bands [5]. The signature splitting and inversion are also important phenomena observed in doubly odd nuclei [6]. Originally, the nucleus ^{134}La was studied in the decay of ^{134}Ce [7]. Two partial level schemes were established by Morek *et al.* [8]. Oliveira *et al.* [9] assigned the configuration $\pi h_{11/2} \otimes \nu h_{11/2}$ to the yrast band. While Pramanik *et al.* [10] proposed six bands, Bark *et al.* [11] made an extensive study of the decay scheme and established five bands. A weakly populated bandlike structure was proposed to be the chiral partner band of the main band, based on $\pi h_{11/2} \otimes \nu h_{11/2}$, by Bark *et al.* [11]. Their claim was based on the similar energy sequence of levels in the two bands. The two other well-established bands are an S band ($\pi g_{7/2} \otimes \nu g_{7/2}h_{11/2}^2$) and an $M1$ band ($\pi h_{11/2} \otimes \nu g_{7/2}h_{11/2}^2$). This strong $M1$ band should be a multiparticle band because of its high value of bandhead spin $12\hbar$ and energy 2.198 MeV. There is, however, no work in the literature establishing the origin of this strong $M1$ band, which could be due to magnetic rotation (shears mechanism). A decrease in $B(M1)$ values with increasing spin needs to be checked in order to establish the shears mechanism of generating the angular momentum. This was the main motivation of our work presented here. In addition, we intended to extend the chiral partner band in order to establish its existence. We performed two experiments: one, to construct the level scheme and determine the lifetime of states

in femtosecond range by the Doppler shift attenuation method (DSAM); another, to find the lifetimes in the picosecond range by the recoil distance method (RDM). As far as the level scheme is concerned, we have added/replaced some transitions. Lifetimes of many states were determined. The $B(M1)$ values for the $M1$ band have been found to be roughly constant with increasing spin up to the backbending region, where there is a sudden increase. This observation ruled out the possibility of magnetic rotation as the mechanism for generating the spins. The theoretical values of $B(M1)$ were estimated from the semiclassical model of Dönau and Frauendorf [12]. Based on the results of these calculations, our results showed the particle configuration to be $\pi g_{7/2} \otimes \nu h_{11/2}(h_{11/2})^2$, which differs from $\pi h_{11/2} \otimes \nu g_{7/2}(h_{11/2})^2$, assigned by Bark *et al.* [11].

II. EXPERIMENTAL DETAILS

To construct the decay scheme and to determine lifetimes by DSAM, an experiment was performed using the heavy-ion fusion reaction $^{124}\text{Sn}(^{14}\text{N}, 4n)^{134}\text{La}$ at the beam energy of 67 MeV, delivered by the Pelletron accelerator at Inter-University Accelerator Centre (IUAC), New Delhi. The target consisted of isotopically enriched (99%) ^{124}Sn of thickness 1.4 mg/cm², rolled with a 10 mg/cm² gold foil. The multi-detector facility, called the γ detector array (GDA), consisting of 12 Compton suppressed coaxial high-purity Ge (HPGe) detectors, and a set of 14 bismuth germanate (BGO) detectors used as a multiplicity filter, was utilized. The HPGe detectors were positioned at the angles θ of 50°, 98°, and 144° with respect to the beam direction.

Initially, the excitation function was measured at various beam energies of 60–70 MeV, and 67 MeV was found to be the optimum energy for the production of ^{134}La . Other important channels were $3n$, $5n$, and $3np$. A twofold and higher coincidence experiment was performed, and the data were collected in the list mode. The total number of collected events was 1.2×10^8 . The information contained in an event

*pragya@phy.iitb.ac.in

was the energy and the time of detection of γ rays with the detector identification and the number of BGO detectors fired, which had the multiplicity information. This multiplicity information was, however, not utilized in our entire data analysis.

The RDM experiment was performed using the reaction $^{124}\text{Sn}(^{15}\text{N}, 5n)^{134}\text{La}$ at a beam energy of 75 MeV. In this experiment, we utilized the ^{15}N beam, and the ^{134}La was populated through the $5n$ reaction channel. This way, we could get a slightly higher recoil velocity of the residues than had been obtained in the first experiment in which the ^{14}N beam was used. The gain in the recoil velocity was due to the higher mass and energy of the projectile. The experimental setup consisted of a plunger inside the GDA setup. The target-stopper assembly was housed in the plunger tube. The stopper could be moved by dc motors, which were controlled remotely by a microcomputer. As a very flat surface was of crucial importance, the Sn target was prepared with special care. Making a self-supporting thin foil by rolling the metallic Sn proved to be very difficult. On the other hand, it was possible to roll Sn along with a supporting material, e.g., Au. For the present work, we used a target of thickness 0.6 mg/cm^2 , with a gold supporter of thickness 2.0 mg/cm^2 . The Au stopper of thickness $\sim 5.0 \text{ mg/cm}^2$ was chosen, which was just enough to stop the residues. The flatness of both the target and the stopper was achieved by the stretching method. The distance between the target and the stopper was measured by the capacitance measurement technique described by Alexander and Forster [13]. The accuracy of this method depended on (i) the flatness and (ii) the parallelism between the target and the stopper. The minimum distance achieved in our experiment was $9 \mu\text{m}$. In total, 16 distances were covered from $9 \mu\text{m}$ to 2 mm . The γ - γ coincidence data were recorded in list mode, and the energy spectra of individual detectors were collected in the singles mode.

III. DATA ANALYSIS AND RESULTS

The energy calibration of the list mode data was done by using the standard radioactive sources ^{152}Eu and ^{133}Ba . The same sources were also utilized to find the relative efficiencies of the HPGe detectors as a function of energy. The list mode data were sorted in $4\text{k} \times 4\text{k}$ matrices of the following types.

- (i) One matrix was E_γ vs E_γ , i.e., the energy of coincident γ rays measured by any two HPGe detectors. This matrix was symmetrized to make the two energy axes equivalent and utilized in generating the projected spectra to construct the level scheme.
- (ii) The other matrix was $E_\gamma(\theta = 98^\circ)$ vs $E_\gamma(\theta = 43^\circ)$, i.e., the energy of the coincident γ rays, one measured by the detectors placed at $\theta = 98^\circ$ and the other measured by the detectors placed at $\theta = 50^\circ$ or $\theta = 144^\circ$ [$\sim 43^\circ$, which was the average of 50° and $(180^\circ - 144^\circ)$]. Only the combination with $\phi = 0^\circ, 180^\circ$ were included. Here, θ is the angle between the detector and the beam direction. The angle ϕ is defined as the angle between two planes, each of which is defined by the detection

direction of the γ ray and the direction of the beam. This matrix was used for finding the directional correlation (DCO) ratios to determine the spins.

- (iii) For the DSAM analysis, three different matrices were created. These were $E_\gamma(\theta = 50^\circ)$ vs $E_\gamma(\theta = \text{any other})$, $E_\gamma(\theta = 98^\circ)$ vs $E_\gamma(\theta = \text{any other})$, and $E_\gamma(\theta = 144^\circ)$ vs $E_\gamma(\theta = \text{any other})$.

A. Decay scheme

The decay scheme was built by finding the coincidence and intensity relationship between various γ rays. The coincidence relations were established by setting gates on the photopeaks of the individual transitions and projecting the coincidence spectra. Gates were also placed on the background in the vicinity of the photopeaks to determine the background contribution to the photopeaks, which were then subtracted from the coincidence spectra. The decrease in the intensity with increasing spin was generally considered. Often the energy sums and differences were used for the placement of γ transitions. In some cases, several gated γ - γ coincidence spectra were summed in order to identify the weak coincidences. The examples of projected spectra with gates on 762, 145, 681, 899, 229, 406, and 611 keV are shown in Fig. 1. These spectra illustrate the presence of new transitions and the replacement of some existing transitions [11]. Figure 1(a) shows the existence of a new transition of energy 474 keV, in addition to the known 476 keV transition. New transitions of 846

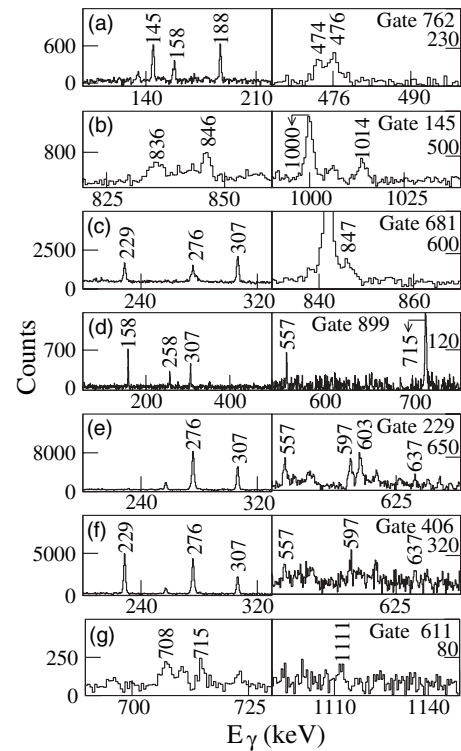


FIG. 1. Projected spectra with gates on (a) 762, (b) 145, (c) 681, (d) 899, (e) 229, (f) 406, and (g) 611 keV transitions. See text for the description.

and 1014 keV are seen in the spectrum with the gate on 145 keV [Fig. 1(b)]. Similarly, a new transition of 847 keV is seen in coincidence with the 681 keV transition [Fig. 1(c)]. We have identified two 557 keV transitions. One of them is a new transition seen in coincidence with the 899 keV transition [Fig. 1(d)], while the other is a known transition [11]. We changed the position of the 603 keV transition because it was not in coincidence with the 406 keV transition [Fig. 1(f)], but it was present in the gated spectrum of the 229 keV transition [Fig. 1(e)]. The placement of the known 708 and 1111 keV transitions was also changed. In the earlier scheme, they were placed parallel to the 611 keV transition. However, we found them to be in coincidence with the 611 keV transition [Fig. 1(g)]. The positions of the 570 and 502 keV transitions were interchanged by assuming that, in general, the intensity of a transition decreases with the increase of angular momentum. Ten transitions, marked with an asterisk (*) in Fig. 2, are either new or replaced, while the remaining decay scheme agrees well with the known scheme [11]. Some known transitions belonging to high excitation energy (shown by dotted arrows) in Fig. 2 could not be observed in our data because of their low intensities.

The multipolarity of the γ transitions was determined by finding the DCO ratio, $R_{\text{DCO}} = \frac{I_{\theta_1}^{\gamma_2}(\text{gate } \theta_2^{\gamma_1})}{I_{\theta_2}^{\gamma_2}(\text{gate } \theta_1^{\gamma_1})}$, where $I_{\theta_i}^{\gamma_2}(\text{gate } \theta_j^{\gamma_1})$ is the intensity of γ_2 detected at θ_i , in coincidence with γ_1 detected at θ_j . The second type of matrix, as mentioned earlier, with angle $\theta_1 = 43^\circ$ on one axis, $\theta_2 = 98^\circ$ on the other axis, and $\phi = 0^\circ$ and 180° , was utilized for this purpose. These angles were chosen to achieve the maximum possible sensitivity in the values of the DCO ratios. The experimentally determined values of the DCO ratios were compared with the theoretical curves to determine the multipolarity of

the transition. The theory of this procedure was based on the prescription given by Krane *et al.* [14]. According to this theory, the nuclei produced in the heavy-ion reaction are aligned in their angular momentum, and the alignment parameter σ measures the degree of alignment. For such nuclei, two coincident γ rays in a cascade, when detected at different angles, show definite patterns in their intensity ratios. These DCO ratios not only depend on the nature of the decaying transitions but also on the mixing ratio δ of both the transitions in the cascade. One of these transitions is normally considered as $E2$ with $\delta = 0$. The calculated DCO curves as a function of δ were plotted for different values of unknown spin I using the alignment parameter value as $\sigma/I = 0.3$. A comparison with the experimental DCO finally decides the unknown spin I . In case there was a multipole mixing, the low value of δ was considered. The general rule of an increase in I with the increasing excitation energy was also adopted. As an example, the unknown spins were assigned to be 9 and 11 in the relevant part of the decay scheme shown in Figs. 3(a) and 3(b), respectively. Only a tentative spin assignment has been done for the new transitions because of their low intensities. The results for all the transitions are summarized in Table I.

B. DSAM analysis

In the DSAM experiment, the target and stopper are completely joined together, with no gap between them. The recoiling nuclei stop either in the target or in the stopper by atomic and nuclear collisions. As the recoiling nuclei slow down in the target and stopper, their velocity changes continuously. This in turn causes Doppler broadening to the energy peaks of γ rays deexciting from the short-lived levels

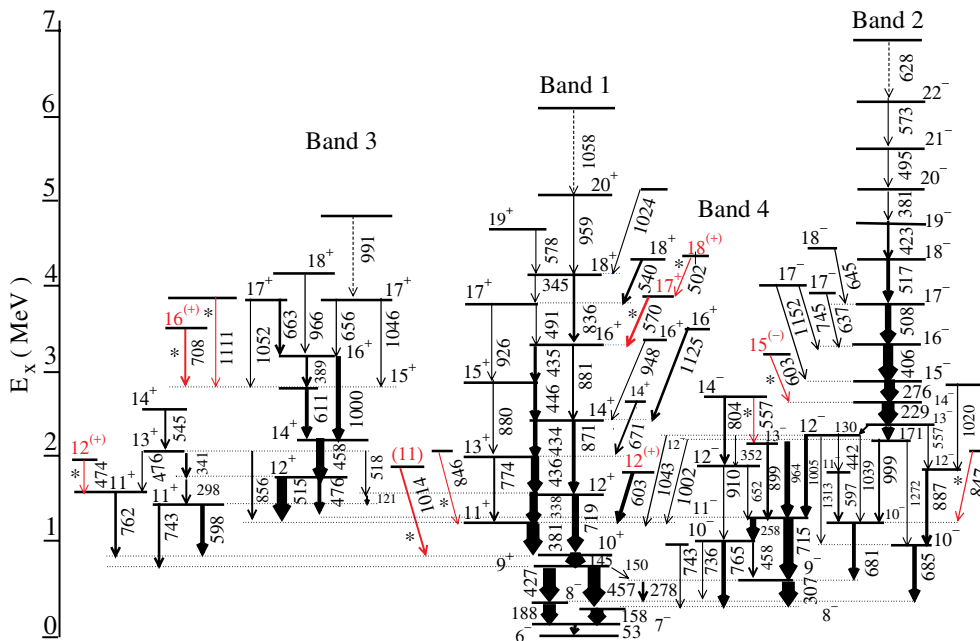


TABLE I. γ -ray energies, spin assignments, and their relative intensities. The uncertainty in the intensity and energy values were estimated to be 5-10% and ± 0.2 keV, respectively. The intensities marked with an asterisk (*) could not be determined accurately because of either contamination or very small values.

E_γ (keV)	I_γ	$I_i(\hbar)$	$I_f(\hbar)$	R_{DCO}	Gate (keV)
53.1	16.12	7 ⁻	6 ⁻	1.16 ± 0.03	188
120.5	5.52	12 ⁺	11 ⁺		
130.3	19.50	13 ⁻	12 ⁻	0.60 ± 0.02	715
144.6	94.05	10 ⁺	9 ⁺	0.33 ± 0.03	719
149.8	*	9 ⁺	9 ⁻		
157.8	100.00	8 ⁻	7 ⁻	0.48 ± 0.03	715
170.6	23.14	13 ⁻	12 ⁻	0.46 ± 0.02	715
187.5	107.00*	8 ⁻	7 ⁻	0.47 ± 0.03	719
228.7	60.47	14 ⁻	13 ⁻	0.62 ± 0.03	715
257.5	24.73	11 ⁻	10 ⁻	0.87 ± 0.03	307
275.8	59.33	15 ⁻	14 ⁻	0.50 ± 0.03	715
278.4	6.21	9 ⁻	8 ⁻		
297.8	7.10	12 ⁺	11 ⁺	0.94 ± 0.05	599
306.5	66.23	9 ⁻	8 ⁻	0.42 ± 0.02	715
337.5	32.07	12 ⁺	11 ⁺	0.47 ± 0.02	871
340.5	9.04	13 ⁺	12 ⁺		
345.4	1.30	18 ⁺	17 ⁺	0.58 ± 0.05	926
352.3	7.43	13 ⁻	12 ⁻		
380.6	5.80	20 ⁻	19 ⁻	0.35 ± 0.04	715
380.9	89.11	11 ⁺	10 ⁺	0.42 ± 0.02	871
389.0	9.53	16 ⁺	15 ⁺	1.10 ± 0.03	611
406.2	39.22	16 ⁻	15 ⁻	0.68 ± 0.05	715
422.5	6.30	19 ⁻	18 ⁻	0.55 ± 0.04	715
427.2	111.25*	9 ⁺	8 ⁻	0.59 ± 0.03	719
434.0	17.74	14 ⁺	13 ⁺		
434.5	12.03	16 ⁺	15 ⁺	0.48 ± 0.03	871
436.0	42.03	13 ⁺	12 ⁺	0.51 ± 0.03	880
441.6	3.21	12 ⁻	11 ⁻		
445.5	15.24	15 ⁺	14 ⁺	0.39 ± 0.03	719
456.7	51.15	9 ⁺	8 ⁻	0.64 ± 0.02	719
457.5	8.13	10 ⁻	9 ⁻		
457.8	32.18	14 ⁺	12 ⁺	0.94 ± 0.02	715
474.0	4.62	12 ⁽⁺⁾	11 ⁺	1.13 ± 0.03	762
476.0	16.31	12 ⁺	11 ⁻	0.53 ± 0.02	715
476.0	5.23	13 ⁺	11 ⁺		
490.7	2.13	17 ⁺	16 ⁺	0.53 ± 0.03	719
494.5	2.53	21 ⁻	20 ⁻	0.66 ± 0.04	715
501.8	2.27	18 ⁽⁺⁾	17 ⁺	0.43 ± 0.05	881
508.2	23.80	17 ⁻	16 ⁻	0.66 ± 0.05	715
515.0	40.33	12 ⁺	11 ⁺	1.02 ± 0.03	145
517.0	16.27	18 ⁻	17 ⁻	0.46 ± 0.06	715
518.0	4.59	13 ⁺	12 ⁺		
539.5	10.04	18 ⁺	17 ⁺	0.89 ± 0.03	491
545.0	7.61	14 ⁺	13 ⁺	1.10 ± 0.03	341
556.7	4.02	13 ⁻	12 ⁻		
557.0	2.00	14 ⁻	13 ⁻		
570.3	11.00	17 ⁺	16 ⁺	1.05 ± 0.03	435
572.7	1.20	22 ⁻	21 ⁻	0.95 ± 0.04	495
577.5	2.50	19 ⁺	18 ⁺	0.52 ± 0.05	836
596.9	6.28	11 ⁻	10 ⁻	0.78 ± 0.04	307
598.2	18.03	11 ⁺	10 ⁺	1.07 ± 0.02	145
602.8	6.50	15 ⁽⁻⁾	14 ⁻	0.94 ± 0.04	229
603.4	20.23	12 ⁽⁺⁾	11 ⁺	1.12 ± 0.03	145
610.6	13.56	15 ⁺	14 ⁺	1.01 ± 0.02	145

TABLE I. (Continued.)

E_γ (keV)	I_γ	$I_i(\hbar)$	$I_f(\hbar)$	R_{DCO}	Gate (keV)
627.5	*		22 ⁻		
636.8	3.80	17 ⁻	16 ⁻	1.04 ± 0.04	229
644.8	5.05	18 ⁻	17 ⁻	1.07 ± 0.04	406
652.1	4.16	12 ⁻	11 ⁻	0.41 ± 0.02	715
655.9	3.42	17 ⁺	16 ⁺	0.58 ± 0.04	1000
662.5	11.25	17 ⁺	16 ⁺	0.42 ± 0.03	1000
670.7	7.07	14 ⁺	13 ⁺	0.41 ± 0.02	719
680.7	16.03	10 ⁻	9 ⁻	1.10 ± 0.02	158
684.7	17.70	10 ⁻	8 ⁻	1.95 ± 0.04	188
707.5	7.11	16 ⁽⁺⁾	15 ⁺	0.92 ± 0.10	611
715.0	39.04	11 ⁻	9 ⁻	2.30 ± 0.03	307
719.1	27.19	12 ⁺	10 ⁺	1.20 ± 0.10	871
735.5	3.12	10 ⁻	8 ⁻		
743.0	4.40		8 ⁻		
743.4	15.00	11 ⁺	9 ⁺	1.96 ± 0.04	188
744.6	10.53	17 ⁻	16 ⁻	1.00 ± 0.03	406
761.6	9.62	11 ⁺	10 ⁺	1.16 ± 0.03	145
764.5	18.00	10 ⁻	8 ⁻	2.65 ± 0.02	158
774.4	6.44	13 ⁺	11 ⁺	1.10 ± 0.05	880
803.7	9.07	14 ⁻	12 ⁻	1.20 ± 0.02	910
835.8	10.00	18 ⁺	16 ⁺	1.00 ± 0.02	881
846.2	2.10		11 ⁺		
846.5	*		10 ⁻		
855.7	6.45	13 ⁺	11 ⁺		
870.8	16.03	14 ⁺	12 ⁺	0.86 ± 0.07	719
879.7	5.21	15 ⁺	13 ⁺	1.11 ± 0.05	926
881.0	7.12	16 ⁺	14 ⁺	0.90 ± 0.05	871
887.2	12.24	12 ⁻	10 ⁻	1.93 ± 0.05	188
898.8	8.04	13 ⁻	11 ⁻	1.09 ± 0.02	715
925.8	2.28	17 ⁺	15 ⁺	0.94 ± 0.05	880
948.1	3.02	16 ⁺	14 ⁺	0.91 ± 0.03	871
958.5	6.03	20 ⁺	18 ⁺	0.88 ± 0.05	836
964.4	22.05	12 ⁻	11 ⁻	0.42 ± 0.03	715
965.6	6.03	18 ⁺	16 ⁺	1.10 ± 0.05	1000
990.9	*		17 ⁺		
998.8	7.04	12 ⁻	10 ⁻	2.10 ± 0.05	307
1000.4	18.12	16 ⁺	14 ⁺	2.10 ± 0.05	663
1002.0	2.10	12 ⁻	11 ⁺		
1005.3	16.18	12 ⁻	11 ⁻	0.42 ± 0.03	715
1013.8	4.20	11	10 ⁺	1.18 ± 0.05	188
1019.5	4.50		12 ⁻		
1024.0	3.32		18 ⁺		
1039.2	8.67	12 ⁻	10 ⁻		
1043.1	4.80	12 ⁻	11 ⁺		
1046.0	3.41	17 ⁺	15 ⁺		
1051.5	*	17 ⁺	15 ⁺		
1111.4	1.36		15 ⁺		
1124.8	7.00	16 ⁺	14 ⁺	0.95 ± 0.04	871
1151.5	3.56	17 ⁻	15 ⁻	2.21 ± 0.12	229
1272.0	1.56	12 ⁻	10 ⁻		
1312.8	3.13	12 ⁻	10 ⁻		

having a lifetime of the order of 10^{-14} to 10^{-12} s. Lifetimes of nuclear states were obtained by comparing the experimental line shapes with the theoretically generated ones. We have done the line shape analysis to extract the lifetimes of several levels in band 2 consisting of $M1$ transitions. As mentioned earlier,

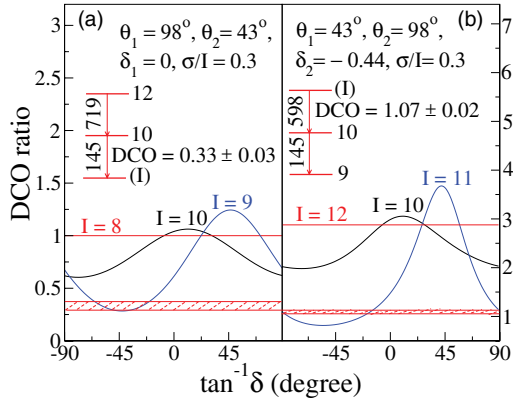


FIG. 3. (Color online) Theoretical DCO curves as a function of δ for coincident γ transitions (a) 719, 145 keV and (b) 598, 145 keV. The hatched region indicates the experimental DCO values.

three matrices with angles $\theta = 50^\circ$, 98° , and 144° on one axis and all the other detectors on the other axis were utilized for the analysis. The line shapes were obtained from the projected spectra by gating on the lower transitions emitted by completely stopped nuclei. This was done for all three angles. These experimental line shapes were fitted with the software code, called LINESHAPE, of Wells and Johnson [15]. The slowing down history of the recoiling nuclei were generated by using the Monte Carlo technique with 5000 histories and a time step of 2 fs. The electronic stopping is treated as a continuous process, while discrete nuclear collisions occur at a rate given by the Lindhart cross section [16]. The feeding intensities and branching ratios were taken from the experimental data. Since the side feeding was unknown, we had to assume a model which represented its time structure as correctly as possible. A five-level side-feeding cascade was adopted for all the levels. Extending or shortening the cascade increased the χ^2 , but did not produce any significant change in the level lifetimes. Starting with the topmost transition in the band, the in-band and side-feeding lifetimes, background parameters, and contaminant-peak parameters were allowed to vary. For each set of these parameters, the simulated line shape was calculated and compared with the experimental spectrum for each angle using the χ^2 minimization program MINUTT [17]. The forward ($\theta = 50^\circ$) and backward ($\theta = 144^\circ$) spectra for each transition were fitted simultaneously. The best-fit background and stopped contaminant-peak parameters were then fixed, and the in-band and side-feeding lifetimes were used as an effective feeding time parameter for the next lower level in the band. Each level was added and fitted in turn, until the entire band was included in a global fit that had independently variable lifetimes for each in-band and side-feeding levels. To limit the contaminants in the gated spectra, it was necessary to use as narrow energy gates as possible. Thus only the clean, fully stopped photopeaks corresponding to the 171, 229, and 276 keV transitions were utilized for the gating purpose. The gating was done on that axis of E_γ - E_γ matrix which corresponds to all the detectors.

Figure 4 shows the summed projected spectra corresponding to the three angles. The data for $\theta = 144^\circ$ were of comparatively poor statistical quality, and some of the peaks,

TABLE II. Mean lifetimes and $B(M1)$ values obtained by DSAM analysis for the states belonging to band 2. Uncertainties in the lifetimes were determined from the behavior of χ^2 in the vicinity of the best-fit parameter values and were propagated through the calculation for the $B(M1)$ strengths. These uncertainties do not include the systematic errors that are associated with the stopping powers, which may be as large as $\pm 20\%$.

E_γ (keV)	States	Mean lifetimes (ps)	$B(M1)$ (μ_N^2)
406.2	$16^- \rightarrow 15^-$	1.76 ± 0.12	$0.48^{+0.03}_{-0.04}$
508.2	$17^- \rightarrow 16^-$	0.93 ± 0.10	$0.47^{+0.05}_{-0.06}$
517.0	$18^- \rightarrow 17^-$	0.90 ± 0.10	$0.46^{+0.05}_{-0.06}$
422.5	$19^- \rightarrow 18^-$	0.89 ± 0.20	$0.85^{+0.15}_{-0.24}$
380.6	$20^- \rightarrow 19^-$	0.40 ± 0.08	$2.58^{+0.43}_{-0.64}$
494.5	$21^- \rightarrow 20^-$	0.28 ± 0.04	$1.68^{+0.21}_{-0.28}$

e.g., $E_\gamma = 495$ keV (Fig. 4), could not be fitted. The position of the unshifted peaks, their full width at half maximum (FWHM), and the variation of FWHM with energy were found from the spectrum of the 98° detector. The contaminants were also located from the same spectrum. Only the statistical error estimated from the line shape fitting has been quoted. The systematic errors associated with the modeling of the stopping powers are not included, and these errors may be as large as 20%. By following this procedure, we found the lifetimes of six levels belonging to band 2 (Fig. 2), and they are presented in Table II. The reduced transition probability $B(M1)$ were calculated using the formula $B(M1) = \frac{0.0569}{E_\gamma^3 \tau(M1)} \mu_N^2$ [18], where the γ -ray energy E_γ is in MeV, and the mean lifetime $\tau(M1)$ of the decaying state is in picoseconds.

C. RDM analysis

The energies of the raw data of all the detectors were initially calibrated. There was no need to do the efficiency correction for finding the intensity ratio $R(= \frac{I_0}{I_0 + I_s})$ as the shifted and unshifted peaks were close in energy. The data from all the detectors at a particular angle were added to get a good statistical quality of the data. The list mode data were analyzed by taking either the total projection or the specific energy gates. The shifted and unshifted peaks were first examined in the total projected spectrum for all the γ lines of interest. In the total projected spectrum, most of the peaks were found to be contaminated or low in intensity and were not clearly seen above the background. Therefore, the specific energy slices were taken to obtain the clean peaks in the projected spectrum. These gated spectra, however, had somewhat low counts in the peaks. The singles mode data were not utilized, as they had excessive unwanted background and contamination. The areas (intensity) of shifted (I_s) and unshifted (I_o) peaks were measured by fitting the peaks to Gaussian shape of adjustable heights and widths. The RADWARE software [19] was utilized for analyzing the energy spectra. A multilevel decay model was assumed while fitting the decay curves. In this model, for the decay of a particular state, the lifetimes of two or three levels above and side-feedings were considered.

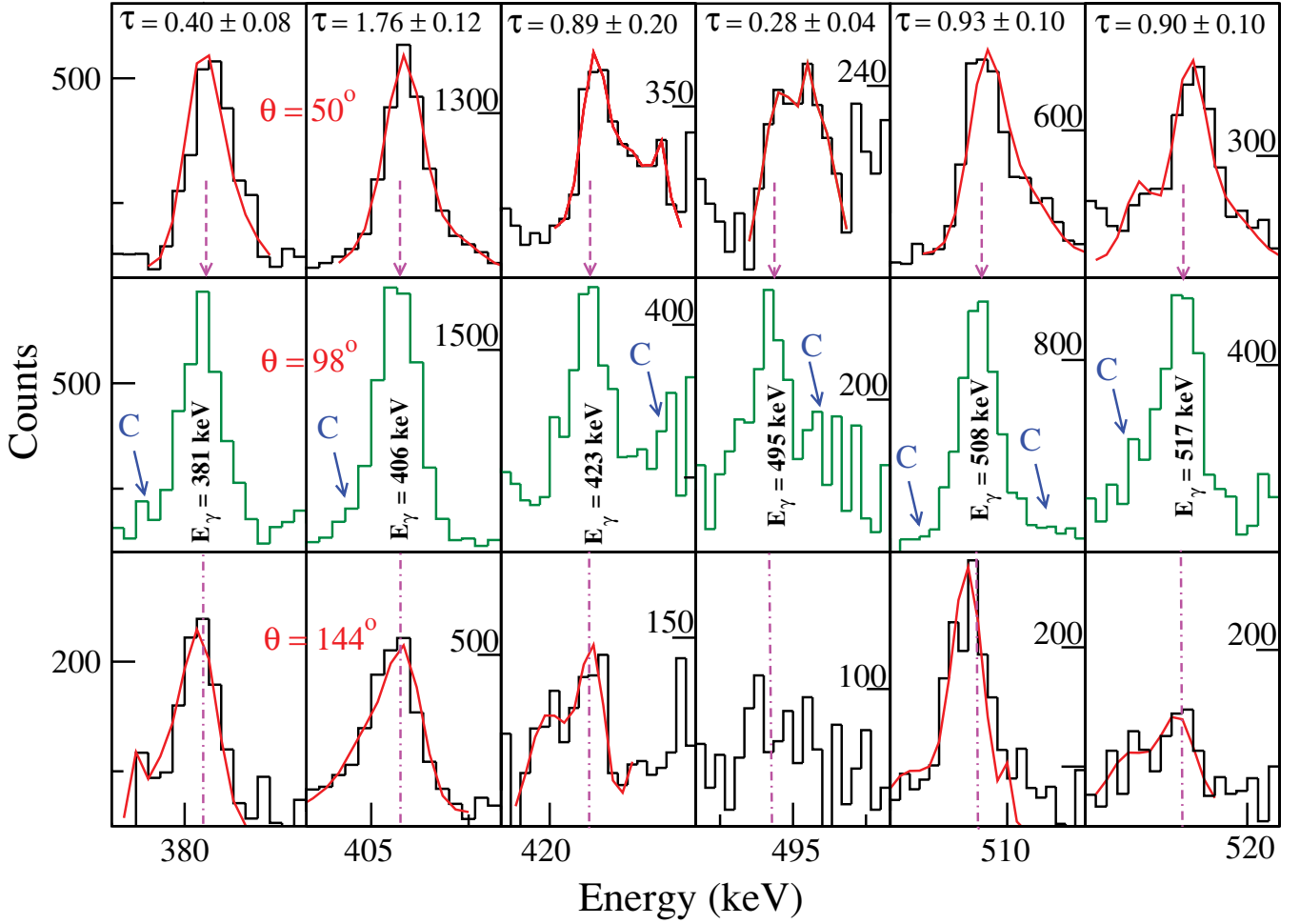


FIG. 4. (Color online) Projected spectra corresponding to three angles, $\theta = 50^\circ$, 98° , and 144° with gates on 171, 229, and 276 keV transitions. The fitting of the line shape is shown with a continuous line for $\theta = 50^\circ$, 144° . The contaminants in the spectra are marked with 'C'.

The experimentally observed intensity values were utilized. Figure 5 shows the projected spectra for the 307 keV ($9^- \rightarrow 8^-$), 381 keV ($11^+ \rightarrow 10^+$), 427 keV ($9^+ \rightarrow 8^-$), 458 keV ($14^+ \rightarrow 12^+$), 515 keV ($12^+ \rightarrow 11^+$), 715 keV ($11^- \rightarrow 9^-$), and 719 keV ($12^+ \rightarrow 10^+$) transitions obtained by gating on 158, 338 + 436, 188, 427, 145 + 427, 307, and 188 + 427 keV transitions, respectively. Figure 6 shows the corresponding decay curves. The long lifetime of the 14^+ state decaying via the 458 keV transition is also reflected in the decay curve of the lower 515 keV transition from the 12^+ state. Table III lists the complete results of the RDM analysis. The quoted error incorporates the fitting error and the error in the average velocity of the recoils, which was assumed to be 7%.

IV. THEORETICAL INTERPRETATION OF $B(M1)$ VALUES

The $B(M1)$ values obtained for band 2 from the DSAM analysis were interpreted by the semiclassical calculations based on the prescription given by Dönau and Frauendorf [12]. There is a close relation between the angular momenta and the

magnetic moment, expressed by the equation

$$\vec{\mu} = g_R \vec{R} + \sum_{\nu} g_{\nu} \vec{j}_{\nu} = g_R \vec{I} + \sum_{\nu} (g_{\nu} - g_R) \vec{j}_{\nu}, \quad (1)$$

where g_{ν} denotes the gyromagnetic ratio of the valence nucleon ν , and g_R is that of the rotation. The total angular momentum

$$\vec{I} = \vec{R} + \sum_{\nu} \vec{j}_{\nu} \quad (2)$$

TABLE III. Mean lifetimes obtained from the RDM experiment.

E_{γ} (keV)	States	Mean lifetimes (ps)
306.5	$9^- \rightarrow 8^-$	86 ± 7
380.9	$11^+ \rightarrow 10^+$	5.7 ± 0.6
427.2	$9^+ \rightarrow 8^-$	216 ± 26
457.8	$14^+ \rightarrow 12^+$	240 ± 36
515.0	$12^+ \rightarrow 11^+$	61 ± 7
715.0	$11^- \rightarrow 9^-$	61 ± 8
719.1	$12^+ \rightarrow 10^+$	3.0 ± 0.6

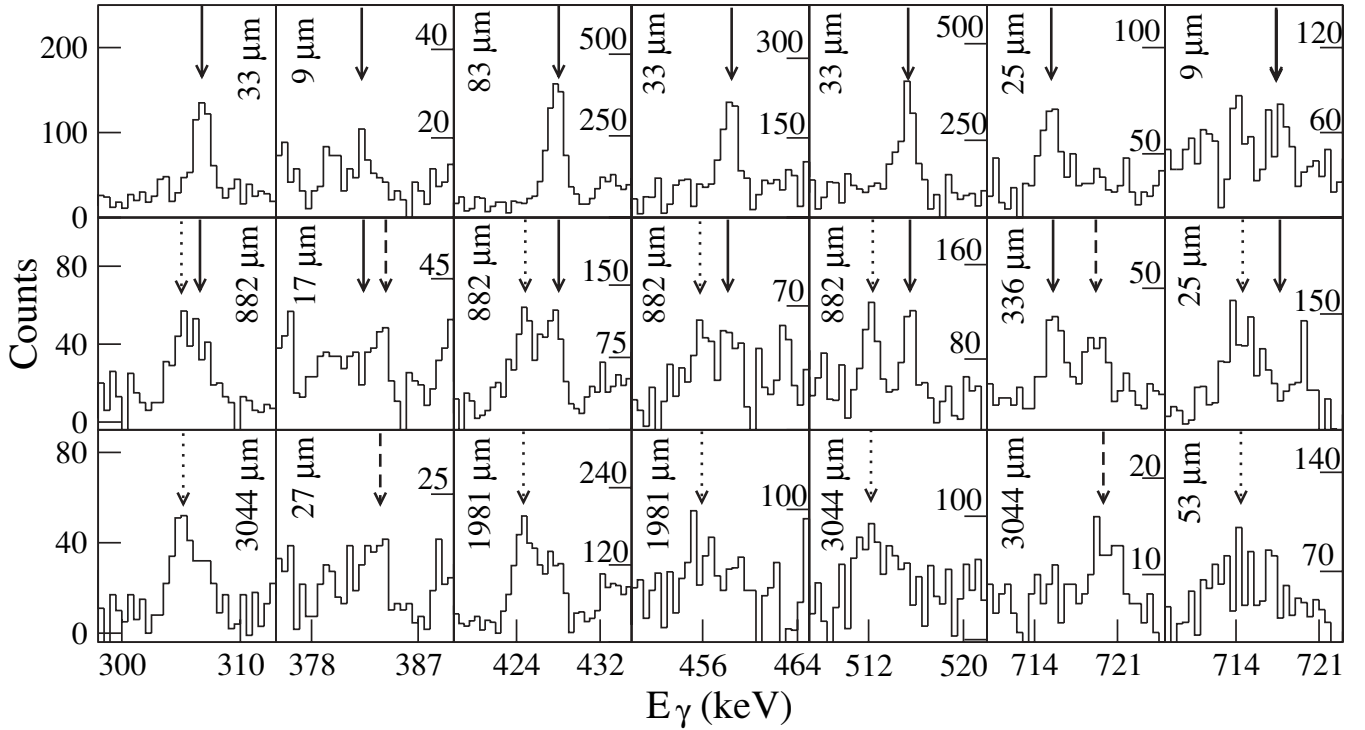


FIG. 5. Shifted and unshifted peaks for 307, 381, 427, 458, 515, 715, and 719 keV transitions. Solid arrow indicates the position of the unshifted peak. Dotted arrow and dashed arrow represent the shifted peaks measured in the backward and forward detectors, respectively.

consists of a collective part \vec{R} and the quasiparticle angular momenta \vec{j}_v . For the rotational gyromagnetic ratio, $g_R \approx Z/A$ was assumed. For quasiparticles belonging to a pure shell with $j = l \pm \frac{1}{2}$, their gyromagnetic ratio g_j is given by the Schmidt value

$$g_j = g_l \pm (g_s - g_l)/(2l + 1). \quad (3)$$

Figure 7 shows a typical example for axial nuclei, where the x axis is the rotation axis, z axis is the symmetry axis, \vec{j}_1 , \vec{j}_2 , and \vec{j}_3 are the particle angular momenta, and \vec{R} is the rotational angular momentum. Since the total angular momentum \vec{I} is conserved in the laboratory frame, all the vectors rotate about the space fixed axis \vec{I} . The particle with angular momentum \vec{j}_3 is assumed to be rotationally aligned. While for \vec{j}_1 and \vec{j}_2 , an intermediate alignment was assumed. Classically, the $M1$ radiation is generated by the magnetic moment $\vec{\mu}$ rotating around the space fixed angular momentum \vec{I} . Thus, the effective component of $\vec{\mu}$ is perpendicular to \vec{I} and is denoted by μ_\perp . The $B(M1)$ values for $\Delta I = 1$ transitions are given by the expression [12,20]

$$B(M1) = (3/8\pi)\mu_\perp^2. \quad (4)$$

From Eq. (1),

$$\mu_\perp = \sum_v (g_v - g_R) j_{v\perp}, \quad (5)$$

where $j_{v\perp}$ is the component perpendicular to \vec{I} . Bark *et al.* [11] theoretically predicted two possible four-quasiparticle (qp) configurations for the negative parity band 2: (i) $\pi g_{7/2} \otimes \nu h_{11/2}(h_{11/2})^2$, which is estimated to be of lowest energy,

and (ii) $\pi h_{11/2} \otimes \nu g_{7/2}(h_{11/2})^2$. These configurations were obtained from the total Routhian surface calculation using the computer program ULTIMATE CRANKER [21,22]. From the experimental data, they estimated the $B(M1)/B(E2)$ values which were consistent with the second configuration $\pi h_{11/2} \otimes \nu g_{7/2}(h_{11/2})^2$. Using the semiclassical model and the angular momentum coupling scheme, shown in Fig. 7, we calculated $B(M1)$ values for both configurations mentioned above. The values of K (projection of \vec{I} on the symmetry axis), i_1 , i_2 , and i_3 (projections of \vec{j}_1 , \vec{j}_2 , and \vec{j}_3 on rotation axis) were taken from the Ref. [11]. K is approximately equal to $K_1 + K_2$, where K_1 and K_2 are, respectively, the projections of \vec{j}_1 and \vec{j}_2 on the symmetry axis. For the configuration $\pi g_{7/2} \otimes \nu h_{11/2}(h_{11/2})^2$, $i_1 \equiv i_\pi = 2.0\hbar$, $i_2 \equiv i_\nu = 3.0\hbar$; and for the configuration $\pi h_{11/2} \otimes \nu g_{7/2}(h_{11/2})^2$, $i_1 \equiv i_\nu = 2.0\hbar$, $i_2 \equiv i_\pi = 3.0\hbar$ were assumed. The directions of \vec{j}_1 and \vec{j}_2 were taken to be approximately the same, consistent with the values of i_1 and i_2 , and two aligned-neutron configuration $\vec{j}_3(\nu h_{11/2})^2$ was considered to be along the rotation axis.

We now explicitly show the calculation for the 4-qp configuration $\pi g_{7/2} \otimes \nu h_{11/2}(h_{11/2})^2$. The total magnetic moment $\vec{\mu}$, given by the components of the odd proton p , odd neutron n , the two aligned neutrons N , and the core R , is written as

$$\vec{\mu} = (g_j^{(p)} - g_R)\vec{j}_p + (g_j^{(n)} - g_R)\vec{j}_n + (g_j^{(N)} - g_R)\vec{j}_N + g_R\vec{I}. \quad (6)$$

The component of $\vec{\mu}$ perpendicular to \vec{I} becomes

$$\mu^\perp = (g_j^{(p)} - g_R)j_p^\perp + (g_j^{(n)} - g_R)j_n^\perp + (g_j^{(N)} - g_R)j_N^\perp. \quad (7)$$

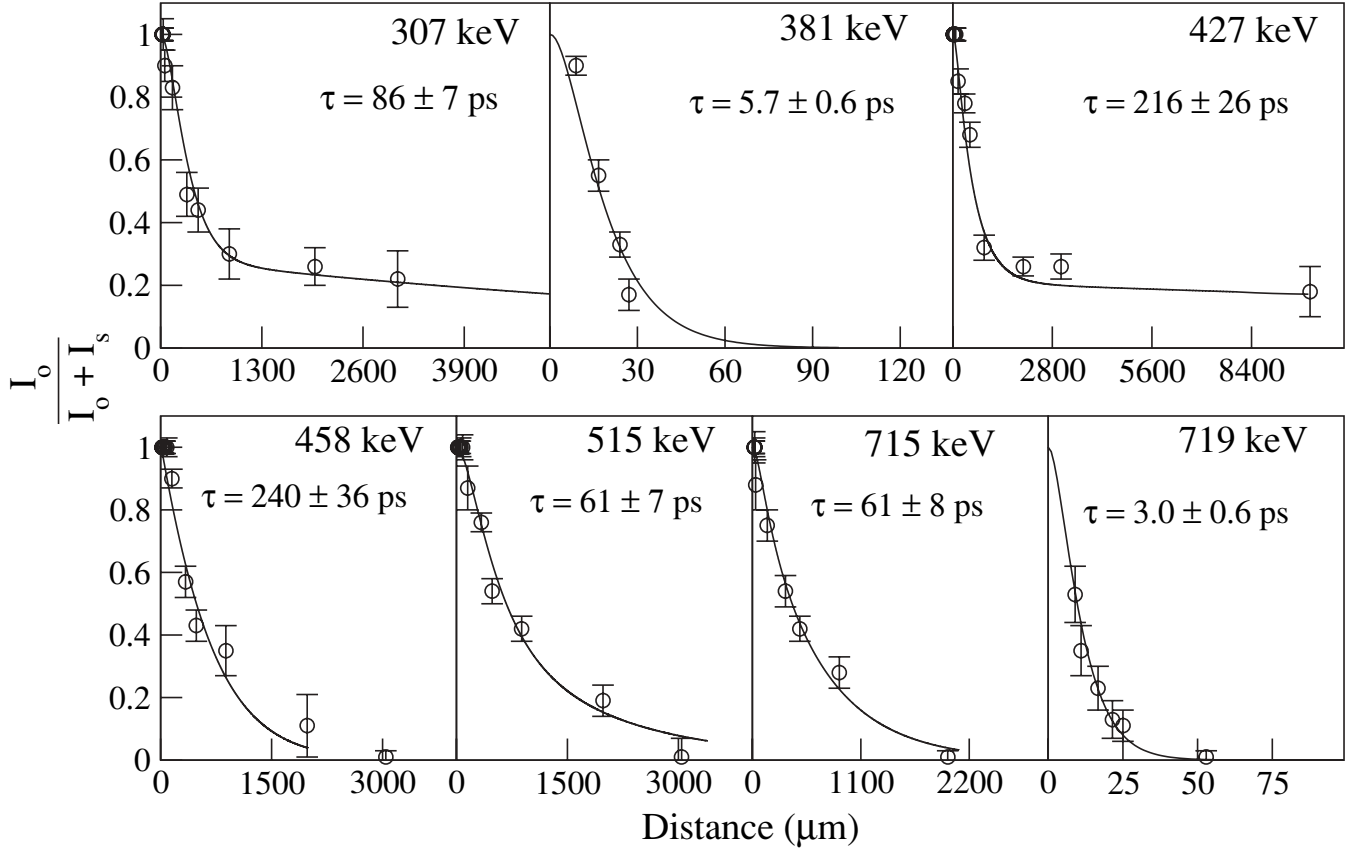


FIG. 6. Decay curves for 307 ($9^- \rightarrow 8^-$), 381 ($11^+ \rightarrow 10^+$), 427 ($9^+ \rightarrow 8^-$), 458 ($14^+ \rightarrow 12^+$), 515 ($12^+ \rightarrow 11^+$), 715 ($11^- \rightarrow 9^-$), and 719 ($12^+ \rightarrow 10^+$) keV transitions obtained from the RDM data analysis.

Using the notations of Fig. 7,

$$\mu^\perp = (g_j^{(p)} - g_R)j_1^\perp + (g_j^{(n)} - g_R)j_2^\perp + (g_j^{(N)} - g_R)j_3^\perp. \quad (8)$$

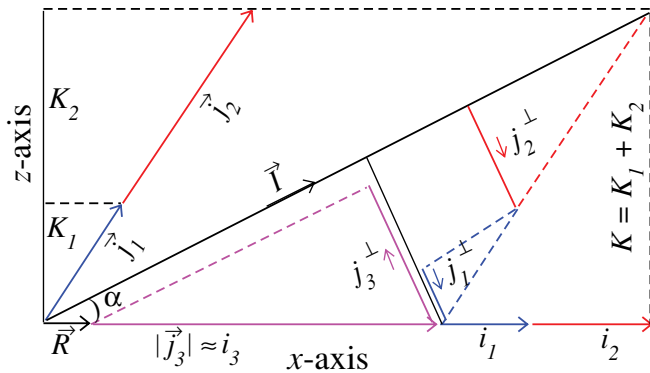


FIG. 7. (Color online) Vector diagram for the four-quasiparticle configuration $\pi g_{7/2} \otimes \nu h_{11/2}(h_{11/2})^2$. The alignment along the rotation axis (x axis) was assumed to be $i_1 = 2\hbar$ and $i_2 = 3\hbar$ for the proton and one neutron, respectively; while two neutrons were considered to be fully rotationally aligned ($i_3 = 9\hbar$). The projection of total angular momentum on the symmetry axis (z axis) was taken to be $K = 5.5$.

Here \vec{j}_1 , \vec{j}_2 , and \vec{j}_3 are the angular momenta corresponding to one proton in $g_{7/2}$, one neutron in $h_{11/2}$, and two aligned neutrons in $(h_{11/2})^2$, respectively. The perpendicular components of angular momenta are

$$j_1^\perp = \frac{j_1}{j_1 + j_2} [(\sqrt{I^2 - K^2} - i_1 - i_2) \sin \alpha], \quad (9)$$

$$j_2^\perp = \frac{j_2}{j_1 + j_2} [(\sqrt{I^2 - K^2} - i_1 - i_2) \sin \alpha], \quad (10)$$

$$j_3^\perp = i_3 \sin \alpha. \quad (11)$$

In these equations,

$$\sin \alpha = \frac{K}{I}. \quad (12)$$

Using g_l^{free} and $0.7g_s^{\text{free}}$, the g_j values for different nucleonic orbits were calculated. These values were $g^p(h_{11/2}) = 1.265$, $g^n(h_{11/2}) = -0.243$, $g^p(g_{7/2}) = 0.677$, and $g^n(g_{7/2}) = 0.298$. The collective value $g_R = Z/A = 0.42$ was used. For $I = 14\hbar$, for example, using the above expressions, we get

$$B(M1) = \frac{3}{8 \times 3.14} \left(\frac{5.5}{14} \right)^2 \left[(0.677 - 0.42) \times (\sqrt{14^2 - 5.5^2} - 5) \frac{7}{18} + (-0.243 - 0.42) \right]$$

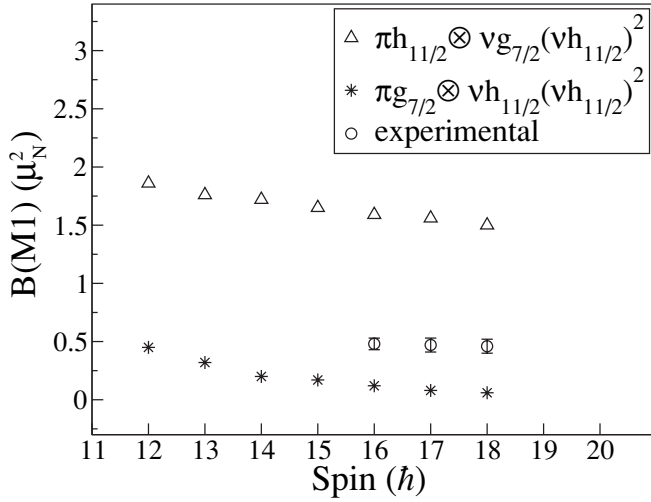


FIG. 8. Calculated $B(M1)$ values for the configurations $\pi h_{11/2} \otimes \nu g_{7/2}(h_{11/2})^2$, assigned by Bark *et al.* [11], and $\pi g_{7/2} \otimes \nu h_{11/2}(h_{11/2})^2$ in comparison with the experimental results. The systematic errors, which are as large as $\pm 20\%$, are not included in the experimental error bars shown here.

$$\times \left(\sqrt{14^2 - 5.5^2} - 5 \right) \frac{11}{18} - (-0.243 - 0.42)9 \Big]^2 = 0.23 \mu_N^2. \quad (13)$$

This value was in reasonable agreement with the experimental value of $\sim 0.47 \mu_N^2$ obtained from lifetime measurements.

Using the same theoretical approach, we calculated the values of $B(M1)$ for two possible configurations $\pi g_{7/2} \otimes \nu h_{11/2}(h_{11/2})^2$ and $\pi h_{11/2} \otimes \nu g_{7/2}(h_{11/2})^2$, and compared them with the experimental results (Fig. 8). The values for the configuration $\pi g_{7/2} \otimes \nu h_{11/2}(h_{11/2})^2$ were found to be the closest to the experimental values. We therefore assigned the multiparticle configuration $\pi g_{7/2} \otimes \nu h_{11/2}(h_{11/2})^2$ to the $M1$ band (band 2). Prior to our measurements, no lifetime data had been available, and the ratios of $B(M1)$ and $B(E2)$ were estimated from the γ -ray intensities by Bark *et al.* [11]. Using the same semiempirical prescription as described here, they calculated the $B(M1)/B(E2)$ ratio and assigned the configuration $\pi h_{11/2} \otimes \nu g_{7/2}(h_{11/2})^2$. In spite of the approximations used in our semiempirical calculations, particularly in considering the various direction of the angular momentum vectors for the particles, we believe that the particle assignment made by them cannot be correct, as that assignment gives too high values of $B(M1)$. Also, the $B(M1)$ values determined directly from the lifetime measurements are

more accurate than the $B(M1)/B(E2)$ found indirectly from the γ -ray intensities. We therefore conclude that the earlier result [11] in assigning the multiparticle configuration to the $M1$ band is incorrect. The $B(M1)$ values remained roughly constant with increasing spin (Table II) and suddenly increased at the backbending region above 18^- . This increase is most likely due to a proton alignment either in $g_{7/2}$ or $h_{11/2}$. A more rigorous calculation based on tilted axis cranking should be performed to explain this.

V. CONCLUSION

The decay scheme of ^{134}La was built using the fusion evaporation reaction $^{124}\text{Sn}(^{14}\text{N}, 4n)^{134}\text{La}$. Five new transitions have been established. The placement of five known transitions in the earlier scheme [11] has been revised. The chiral partner band of $\pi h_{11/2} \otimes \nu h_{11/2}$ could not be extended beyond that proposed by Bark *et al.* Using the RDM and DSAM techniques, lifetimes of 13 different states, in the picosecond and subpicosecond ranges, have been determined. Lifetimes of seven of these states, obtained from RDM measurements, belonged to low-lying excited states. With the DSAM data analysis, the lifetimes of six states belonging to a strong $M1$ band were determined. Roughly constant values of $B(M1)$ were found up to the backbending region. Therefore, the possibility of this band being a magnetically rotating band is ruled out. The semiempirical formalism was utilized to find the theoretical values of $B(M1)$, and the multiparticle configuration $\pi g_{7/2} \otimes \nu h_{11/2}(h_{11/2})^2$ was assigned to this band. Our assignment is at variance with the work of Bark *et al.* [11], who assigned the configuration $\pi h_{11/2} \otimes \nu g_{7/2}(h_{11/2})^2$, based solely on the intensities of γ rays.

ACKNOWLEDGMENTS

The help provided by Deepa Thapa and S. Mahadkar in preparing the targets is gratefully acknowledged. The full cooperation of the Pelletron staff at IUAC for the smooth running of the experiment is also thankfully acknowledged. This work was financially supported by a research grant (project no. 20/2/97-R&D II/607) from the Board of Research on Nuclear Sciences (BRNS). Vinod Kumar acknowledges the financial support, in the form of a senior research grant, provided by the Council of Scientific and Industrial Research (CSIR), New Delhi.

- [1] S. Juutinen, P. Simecek, P. Ahonen, M. Carpenter, C. Fahlander, J. Gascon, R. Julin, A. Lampinen, T. Lonnroth, J. Nyberg, A. Pakkanen, M. Piiparinen, K. Schiffer, G. Sletten, S. Tormanen, and A. Virtanen, Phys. Rev. C **51**, 1699 (1995).
- [2] C. M. Petrache, G. de Angelis, D. Bucurescu, M. Ivascu, D. Bazzacco, and S. Lunardi, Z. Phys. A **344**, 227 (1992).
- [3] E. S. Paul, C. W. Beausang, D. B. Fossan, R. Ma, W. F. Piel, Jr., N. Xu, L. Hildingsson, and G. A. Leander, Phys. Rev. Lett. **58**, 984 (1987).

- [4] E. Grodner, J. Srebrny, A. A. Pasternak, I. Zalewska, T. Morek, Ch. Droste, J. Mierzejewski, M. Kowalczyk, J. Kownacki, M. Kisielinski, S. G. Rohozinski, T. Koike, K. Starosta, A. Kordyasz, P. J. Napiorkowski, M. Wolinska-Cichocka, E. Ruchowska, W. Plociennik, and J. Perkowski, Phys. Rev. Lett. **97**, 172501 (2006).
- [5] S. Lakshmi, H. C. Jain, P. K. Joshi, A. K. Jain, and S. S. Malik, Phys. Rev. C **69**, 014319 (2004).

- [6] H. J. Chantler, E. S. Paul, A. J. Boston, M. P. Carpenter, R. Charity, C. J. Chiara, P. T. W. Choy, C. N. Davids, M. Devlin, A. M. Fletcher, D. B. Fossan, D. G. Jenkins, N. S. Kelsall, T. Koike, D. R. LaFosse, P. J. Nolan, D. G. Sarantites, D. Seweryniak, J. F. Smith, K. Starosta, R. Wadsworth, and A. N. Wilson, *Phys. Rev. C* **66**, 014311 (2002).
- [7] R. C. Greenwood, R. J. Gehrke, R. G. Helmer, and C. W. Reich, *Nucl. Phys.* **A270**, 29 (1976).
- [8] T. Morek, H. Beuscher, B. Bochev, T. Kutsarova, R. M. Lieder, M. Muller-Veggian, and A. Neskakis, *Nucl. Phys.* **A433**, 159 (1985).
- [9] J. R. B. Oliveira, L. G. R. Emediato, E. W. Cybulska, R. V. Ribas, W. A. Seale, M. N. Rao, N. H. Medina, M. A. Rizzutto, S. Botelho, and C. L. Lima, *Phys. Rev. C* **45**, 2740 (1992).
- [10] U. D. Pramanik, A. Mukherjee, A. K. Singh, S. Chattopadhyay, G. Gangopadhyay, A. Goswami, M. S. Sarkar, R. K. Bhowmik, R. P. Singh, S. Muralithar, B. Dasmahapatra, S. Sen, and S. Bhattacharya, *Nucl. Phys.* **A632**, 307 (1998).
- [11] R. A. Bark, A. M. Baxter, A. P. Byrne, G. D. Dracoulis, T. Kibedi, T. R. McGoram, and S. M. Mullins, *Nucl. Phys.* **A691**, 577 (2001).
- [12] F. Dönaue and S. Frauendorf, in *Proceedings of the International Conference on High Angular Momentum Properties of Nuclei, Oak Ridge, 1982*, edited by N. R. Johnson (Harwood, New York, 1983), p. 143.
- [13] T. K. Alexander and J. S. Forster, in *Advances in Nuclear Physics*, edited by Michel Baranger and Erich Vogt (Plenum, New York, 1978), Vol. 10, Chap. 3.
- [14] K. S. Krane, R. M. Steffen, and R. M. Wheeler, *Nucl. Data Tables* **A11**, 351 (1973).
- [15] J. C. Wells and N. Johnson (private communication).
- [16] J. Lindhard, M. Scharff, and H. E. Schiott, *Mat. Fys. Medd. Dan. Vid. Selsk.* **33**, 14 (1963).
- [17] F. James and M. Roos, *Comput. Phys. Commun.* **10**, 343 (1975).
- [18] P. Ring and P. Schuck, *The Nuclear Many-Body Problem* (Springer-Verlag, Heidelberg, 1980).
- [19] D. C. Radford, *Nucl. Instrum. Methods Phys. Res. A* **361**, 297 (1995).
- [20] F. Dönaue, *Nucl. Phys.* **A471**, 469 (1987).
- [21] T. Bengtsson, *Nucl. Phys.* **A496**, 56 (1989).
- [22] R. Bengtsson, T. Bengtsson, M. Bergström, H. Ryde, and G. B. Hagemann, *Nucl. Phys.* **A569**, 469 (1994).